Enhanced flow in deformable carbon nanotubes

Ashish Garg[1,2,3*]
[1]Seminare Private Limited, Delhi, India
[2]Department of Chemical Engineering, Indian Institute of Technology Delhi, India
[3]Department of Mechanical & Aerospace Engineering, NIMS University, Jaipur, India
October 26, 2023

Abstract

Water transport through nanopores is widespread in the natural world and holds significant implications in various technological applications. Several researchers observed a significant increase in water flow through graphene-based nanotubes. Graphene sheets are deformable, so we represent nano/Angstrom-size tubes with a deformable wall model using the small displacement structural mechanics with a linear pressure-area relationship. We assume the lubrication assumption in the shallow tubes, and using the microstructure of confined water along with slip at the capillary boundaries, we derive the model for deformable nanotubes. Our derived model also facilitates the flow dynamics of Newtonian fluids under different conditions as its limiting cases, which have been previously reported in the literature. We compare the predictions by our deformable-wall and rigid-wall model with the experimental results and the MD simulation predictions by multiple literatures. Many studies were well-predicted by the rigid-wall model with slips. However, we find that there are many studies with high porosity and thin wall tubes, where elasticity or deformability of the tube is essential in modelling, which is well-predicted by our deformable-wall model with slips. In our study, we focus on investigating the impact of two key factors: the deformability of the nanotubes and the slip length on the flow rate. We find that the flow rate inside the tube increases as the deformability $1/\alpha$ increases (or corresponding thickness $\mathcal{T}$ and elastic modulus E of the wall decreases). We find that the flow rate in deformable tubes scales as $\dot{m}_{\text{deformable}} \sim 1/\alpha^0$ for $\left(\Delta p/\alpha A_o\right) \ll 1$, $\dot{m}_{\text{deformable}} \sim 1/\alpha$ for $\left(\Delta p/\alpha A_o\right) \sim O(10^{-1})$ and $\dot{m}_{\text{deformable}} \sim \alpha^2$ for $\left(\Delta p/\alpha A_o\right) \sim O(1)$. We also find that, for a given deformability factor α, the percentage change in flow rate in the smaller diameter of the tube is much larger than the larger diameter. As the tube diameter decreases for the given reservoir pressure, $\Delta\dot{m}/\dot{m}$ increases A_o^{-1} followed by A_o^{-2} after a threshold with the tube diameter. We find that for the rigid tube, where the deformability parameter $1/\alpha = 0$, the mass flow rate varies linearly, i.e., $\dot{m}_{\text{rigid}} \sim \Delta p$, whereas for the deformable tubes, the flow rate scales as $\dot{m}_{\text{deformable}} \sim \Delta p^2$ for $\left(\Delta p/\alpha A_o\right) \sim O(10^{-1})$ during transition from $\dot{m}_{\text{rigid}} \sim \Delta p$ to $\sim \Delta p^3$, and finally to $\dot{m}_{\text{deformable}} \sim \Delta p^3$ for $\left(\Delta p/\alpha A_o\right) \sim O(1)$. We further find that the slip also significantly increases the mass flow rate in the nanotubes. Still, the deformability has, in comparison, a more substantial effect in increasing the mass flow rate to several orders than the slips.

*Email: **ashish.garg.iisc@gmail.com, ashish@seminare.in**

Submitted

Keywords: deformable nanotubes, nano/Angstrom-size capillaries, lubrication approximation, linear pressure-area relation, nanoconfined water

1 Introduction

The study of water's transport behavior within nanopores holds considerable importance in terms of fundamental understanding and practical applications. This significance arises from the widespread occurrence of nanopores in nature and has numerous technological uses [1–9]. For example, in the natural world, plants absorb water through nanocapillaries [10, 11]. Also, from a technological perspective, the utility of nanocapillary flow has been harnessed in diverse applications. Prominent instances encompass deformable nanotubes within lab-on-a-chip devices, which enable precise manipulation and analysis of minute fluid volumes [12, 13]. These pliable nanotubes facilitate the creation of miniaturized systems, serving purposes such as chemical and biological sensing, DNA sequencing, and drug delivery [14–16]. Furthermore, the employment of deformable nanotubes in processes like water purification, desalination, filtration, and the separation of biomolecules is driven by their selective permeability, allowing specific molecules or particles to pass through while impeding others [17, 18]. Also, given their large surface area and the controlled channeling of water flow, deformable nanotubes find application in heat exchange systems to enhance the efficiency of cooling processes [19–22].

Several researchers observed a significant increase in water flow through graphene-based nanotubes [8, 9, 23–25]. Many of those researchers employed a hybrid approach, combining the Hagen-Poiseuille theory [26, 27] under the continuum modeling of nanoconfined water properties and molecular dynamic simulations to investigate capillary and transport behavior in nanotubes. They represented the capillaries as rigid wall nanotubes and presented a model for the mass flow rate. They linked the rapid nanoconfined water flow to water molecules' elevated density, viscosity, or considerable slip lengths within nano capillaries. The characteristics of water flow in highly confined nanoscale environments continue to be a subject of fascination, with some researchers suggesting further significantly increased flow rates that remain unresolved even after applying substantial slip effects [23, 25, 28–33].

Given the deformable nature of Graphene sheets [34], the flexibility of a narrow carbon nanotube (CNT) plays a pivotal role in influencing both the effective pressure drop across the tube and the resultant flow pattern [35, 36]. This is primarily because the flow rate is susceptible to the cross-section's length scale, demonstrating a third-power dependence [35]. Consequently, even minor alterations in the tube's geometry can lead to substantial changes in the system's pressure drop and flow characteristics. To address this, in this paper, we adopt a small displacement structural mechanics approach with a linear pressure-area relationship, as introduced by Sochi [35], to model these graphene-based nanotubes as deformable structures.

Under the lubrication approximation in the shallow nanotubes (specifically, the ratio of the tube's diameter to its length is assumed small), and using the microstructure of nanoconfined water along with slip at the capillary boundaries, we study the effect of deformability of nanotube to the flow rate. We compare predicted flow rates considering both the tube's deformability and the application of slips with the experimental findings and the molecular dynamic simulations

results from multiple literature [8, 9, 23–25, 28–33]. We also compare the same with the rigid-wall model as well in this paper.

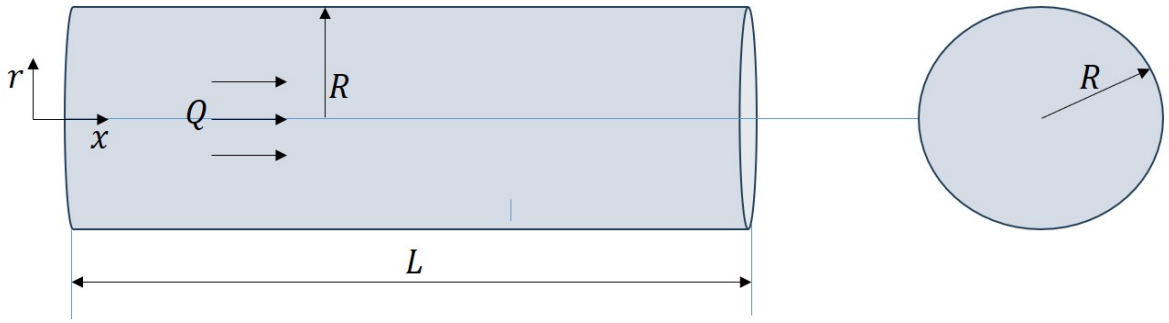

Figure 1: Schematic diagram of the flow Q in a graphene deformable-wall nanotube with length L and the cross-section radius R (diameter D).

We consider a shallow nanotube with a length L and radius R (diameter D), satisfying the condition $D \ll L$ as shown in figure 1. The tube's wall is deformable. The flow Q because of the applied pressure field occurs along the x-direction. As a result of the normal stresses exerted by the flow on the walls, the soft wall of the tube deforms radially. A pressure field p is applied at the reservoir at $x = 0$, and the exit pressure is assumed to be zero for reference purposes. Currently, we do not assume any particular magnitude for the deformable displacement. Still, we anticipate the magnitude $|\delta| \ll D$ in our problem, where δ is the change in radius due to wall deformation, i.e., $R = R_o + \delta$, where R_o is the initial or rigid wall tube radius and R is the radius after tube-wall deformation. The structure of the paper is outlined as follows. Section 2 describes the the governing equations, while Section 3 presents the model's derivation. In the Section 4, we present and analyze the results. Finally, we present conclusions in Section 5.

2 Governing equations

2.1 Cauchy equations

The Cauchy's equation and the continuity equation for an incompressible fluid are given by

$$\rho\left(\frac{\partial \boldsymbol{v}}{\partial t} + (\boldsymbol{v}\cdot\boldsymbol{\nabla})\boldsymbol{v}\right) = -\boldsymbol{\nabla}p - \rho\boldsymbol{g} + \boldsymbol{\nabla}.\boldsymbol{\tau}, \qquad \boldsymbol{\nabla}\cdot\boldsymbol{v} = 0, \tag{1a,b}$$

where $\boldsymbol{v} = [u \quad u_r \quad u_\theta]$ is the fluid velocity with u along axial direction, u_r along radial direction, and u_θ along azimuthal direction. Also, p is the fluid pressure, ρ is the fluid density, $\boldsymbol{g}$ is the gravitational body force, and $\boldsymbol{\tau}$ is the total deviatoric stress tensor. We use a cylindrical coordinate system (x,r, θ) with r and x orientated radially and along the centreline of the tube. We assume axisymmetry flow field, i.e. $\dfrac{\partial}{\partial\theta}() = 0$.

2.1.1 Boundary conditions

Boundary conditions play an essential role in determining the solution. We assume that the fluid cannot penetrate the tube's wall therefore, on the boundary Γ, it gives

$$\boldsymbol{v} \cdot \boldsymbol{n}_{\text{wall}} = 0, \tag{2}$$

where $\boldsymbol{n}_{\text{wall}}$ is the unit outward normal vector on the wall. Generally, the no-slip boundary condition at the fluid-solid interface is common in fluid mechanics. However, fluid flow at the nano and Angstrom scale require a certain degree of tangential velocity (Navier slip) to match experimental observations [37–40]. This leads to

$$\boldsymbol{v}.\boldsymbol{m}_{\text{wall}} = \lambda|\boldsymbol{v_g}|, \tag{3}$$

where $\boldsymbol{m}_{\text{wall}}$ is the tangential unit vector along the wall. Also, the arbitrary parameter λ is the slip length, and $\boldsymbol{v_g}$ is the tangential velocity gradient with the normal direction.

The symmetry boundary condition at the centreline of the tube $r = 0$ demands the velocity normal to the centreline, and the Cauchy traction vector $\boldsymbol{t}$ tangential to the centreline is zero. These two conditions can be expressed as

$$\boldsymbol{v} \cdot \boldsymbol{n}_{\text{centreline}} = 0, \tag{4}$$

and

$$\boldsymbol{t} \cdot \boldsymbol{m}_{\text{centreline}} = 0, \tag{5}$$

respectively, where $\boldsymbol{n}_{\text{centreline}}$ and $\boldsymbol{m}_{\text{centreline}}$ are the unit normal and unit tangent vector to the centreline boundary, respectively. The traction on the boundary, which is equivalent to a Neumann boundary condition, is expressed as

$$\boldsymbol{t} = (-p\boldsymbol{I} + \boldsymbol{\tau})\boldsymbol{n}_{\text{centreline}}. \tag{6}$$

3 The Axisymmetric model: Involving microstructure of confined water

3.1 Structural small displacement mechanics: A linear pressure-area relationship

Many models describe the relationship between local pressure and local cross-sectional area in deformable tubes [35]. In this paper, we use a simple linear Pressure-Area correlation model

$$p = \alpha(A - A_o) \tag{7}$$

to derive the axisymmetric model [35]. This model assumes a linear correlation between pressure p and the change in cross-sectional area $A - A_o$. Here, α represents the proportionality factor, which indicates the stiffness of the tube wall. A is the tube's cross-sectional area at the actual pressure p, and A_o is the initial tube area (or rigid tube-wall area) at the reference pressure (assumed to be zero for convenience). The model essentially states that the change in pressure at a specific point within the tube is directly proportional to the change in the cross-sectional area relative to its reference state.

3.2 Axisymmetric model

We consider fully developed, axisymmetric, steady, incompressible laminar flow in a circular deformable tube of radius R (Diameter D) as shown in the schematic diagram (figure 1). The tube is assumed to be sufficiently long in comparison to the radius (i.e., $R/L \ll 1$, to use a two-dimensional axisymmetric model [41, 42]. We also exclude any hydrodynamic instability caused by deformable walls in the transience flow field. We further assume a very small expansion δ due to deformability in comparison to the radius of the tube, $\delta/R \ll 1$, which is caused by the pressure difference between the fluid and the atmospheric conditions in the deformable tube.

We assume the cylindrical velocity components u and u_r along longitudinal and radial directions x and r, respectively. The r coordinate is measured from the centre of the tube. Therefore, assuming a fully developed, axisymmetric, steady, incompressible laminar flow in a circular deformable tube and using the impermeable solid-wall boundary condition, which is $u_r(r = R) = 0$, we get the radial velocity vanishes everywhere, i.e.

$$u_r(r, t) = 0. \tag{8}$$

Also, we neglect all body forces, such as gravitational forces over capillary forces. Under these assumptions for $R/L \ll 1$, the Cauchy's equation (1)(a) can be written as

$$\begin{aligned} 0 &= -\frac{1}{\rho}\frac{\partial p}{\partial x} + \frac{\eta}{\rho}\frac{1}{r}\frac{\partial}{\partial r}\left(r\frac{\partial u}{\partial r}\right), \\ 0 &= -\frac{\partial p}{\partial r}, \end{aligned} \tag{9}$$

where η and ρ are the viscosity and density of confined water, respectively. Using the Navier slip, the tangential solid-wall boundary condition gives

$$u(r = R) = \lambda\left|\frac{\partial u}{\partial r}\right|, \tag{10}$$

where $\lambda \geq 0$, is the slip length [43]. Further integrating equation (9), we get

$$u = \frac{\partial p}{\partial x}\frac{r^2}{4\eta} + c_1 \ln r + c_2, \tag{11}$$

where c_1 and c_2 are the integration constant. Since u needs to be finite at $r = 0$, this implies $c_1 = 0$. From equation (10), the slip boundary condition at the tube wall yields

$$c_2 = \lambda\left|\frac{\partial p}{\partial x}\frac{R}{2\eta}\right| - \frac{\partial p}{\partial x}\frac{R^2}{4\eta}. \tag{12}$$

Upon substitution, we get

$$u = -\frac{\partial p}{\partial x}\frac{1}{4\eta}(R^2 - r^2) + \lambda\left|\frac{\partial p}{\partial x}\frac{R}{2\eta}\right|. \tag{13}$$

The volume flow rate in a deformable nanotube is given by

$$Q = \int_0^{R(x)} u\ 2\pi\ r\ dr = -\frac{\partial p}{\partial x}\frac{\pi R^4}{8\eta} - \lambda\pi\frac{\partial p}{\partial x}\frac{R^3}{2\eta}. \tag{14}$$

As we know from equation (7), that

$$A = \frac{p}{\alpha} + A_o, \tag{15}$$

where $A = \pi R^2$, and $A_o = \pi R_o^2$. Substituting equation (15) in equation (14), we get

$$Q = -\frac{\partial p}{\partial x}\left[\frac{1}{8\pi\eta}\left(\frac{p}{\alpha} + A_o\right)^2 + \lambda\frac{1}{2\eta\sqrt{\pi}}\left(\frac{p}{\alpha} + A_o\right)^{3/2}\right]. \tag{16}$$

We assume $p(x = 0)$ to be the relative inlet pressure with respect to the pressure at the tube outlet, i.e., $p(x = L) = 0$. In nano and Angstrom scale tubes, the viscosity $\eta(D)$ and density $\rho(D)$ is a function of the diameter of the tube [44]. Under small displacements of the wall, we assume the viscosity and density to be $\eta(R) \sim \eta(R_o)$, and $\rho(R) \sim \rho(R_o)$, respectively. We integrate equation (16) along the tube length L, which yields

$$\int_x^L Q dx = \int_0^{p(x)} \left[\frac{1}{8\pi\eta}\left(\frac{p}{\alpha} + A_o\right)^2 + \lambda\frac{1}{2\eta\sqrt{\pi}}\left(\frac{p}{\alpha} + A_o\right)^{3/2}\right] dp, \tag{17}$$

$$\implies (L - x)Q = \frac{\alpha}{24\pi\eta}\left[\left(\frac{p}{\alpha} + A_o\right)^3 - A_o^3\right] + \lambda\alpha\frac{1}{5\eta\sqrt{\pi}}\left[\left(\frac{p}{\alpha} + A_o\right)^{5/2} - A_o^{5/2}\right]. \tag{18}$$

As the flow rate Q is not a function of longitudinal directional. Therefore substituting $x = 0$ in equation (18) gives the volume flow rate in the tube as

$$Q = \frac{1}{L}\left(\frac{\alpha}{24\pi\eta}\left[\left(\frac{\Delta p}{\alpha} + A_o\right)^3 - A_o^3\right] + \lambda\alpha\frac{1}{5\eta\sqrt{\pi}}\left[\left(\frac{\Delta p}{\alpha} + A_o\right)^{5/2} - A_o^{5/2}\right]\right), \tag{19}$$

where $p(x = 0) = \Delta p$. Therefore the mass flow rate can be written as

$$\dot{m}_{\text{deformable}} = \rho Q = \frac{\rho(D)}{\eta(D)\ L}\left(\frac{\alpha}{24\pi}\left[\left(\frac{\Delta p}{\alpha} + A_o\right)^3 - A_o^3\right] + \lambda\alpha\frac{1}{5\sqrt{\pi}}\left[\left(\frac{\Delta p}{\alpha} + A_o\right)^{5/2} - A_o^{5/2}\right]\right), \tag{20}$$

where $\rho(D)$, and $\eta(D)$ are the density and viscosity of nanoconfined water, which are the function of the diameter of the tube as explained in the following section 3.3.

3.3 Microstructure of confined water

Many investigations have highlighted the impact of tube diameter on essential fluid properties [9, 24, 45–49]. Moreover, these researchers have employed diverse models and equations to fit density, viscosity, and slip length data, leading to a certain level of confusion and making it

challenging to determine which model is most suitable for incorporation into modeling and numerical simulations [50–52]. To address this uncertainty, Garg and Bishnoi [53] paper presents a unified model that can be employed to characterize density, viscosity, and slip length in nanoscale confined tubes. Using the density, viscosity, and slip length models from Garg and Bishnoi [53] such as for density

$$\frac{\rho(D)}{\rho_o} = a + \frac{b}{(D-c)^n}, \tag{21}$$

where $\rho(D)$ is the tube's diameter-dependent fluid density. The ρ_o is the bulk density at $D \implies \infty$. a, b, c are the free parameter. The power-law index n shows the diameter dependence. As D tends to infinity, the density ratio approaches a constant value a, whereas if $a = 1$, it approaches a regular bulk density value. For viscosity, we use

$$\frac{\eta(D)}{\eta_o} = a + \frac{b}{(D-c)^n}, \tag{22}$$

where $\eta(D)$ is the tube's diameter-dependent viscosity of the fluid. The η_o is the bulk viscosity at $D \implies \infty$. a, b, c are the free parameters and capture the specific behavior of the fluid's viscosity in confinement. The power-law index n shows the diameter dependence. In this paper, we use Ye et al. [44] nanoconfined density and viscosity at 298 K. We model for tube diameter $D \geq 25$ Å in this study, for that, the slip length is constant and from multiple studies including Ye et al. [44], the constant value is reported between 50nm to 300nm. In order to model Ye et al. [44] nanoconfined density data at temperature 298 K as shown by Garg and Bishnoi [53] in green color solid-line, they get $\rho_o = 1000$ kg/m^3, $a = 1$, $b = -7.96$ X 10^{-10} m, $c = -1$ X 10^{-10} m, and $n = 1$. Also, to model the Ye et al. [44] nanoconfined viscosity data at temperature 298 K as shown by Garg and Bishnoi [53] on the solid-green line, they get $\eta_o = 1$ mPa-s, $a = 0.9$, $b = -3.21$ X 10^{-10} m, $c = 1$ X 10^{-10} m, and $n = 1$. Under small displacements of the tube wall, we assume the density and viscosity to be $\rho(D) \sim \rho(D_o)$ and $\eta(D) \sim \eta(D_o)$, respectively. We model the flow rate in deformable nanotubes using these experimental parameters in the following section 4.

4 Results and discussion

Using equations (20), the mass flow rate for the deformable wall N carbon tubes using the microstructure properties of confined water can be written as

$$\dot{m}_{\text{deformable}} = \rho N Q = \frac{N\rho(D_o)}{\eta(D_o)\ L}\left(\frac{\Delta p\ A_o^2}{8\pi}\left[\frac{1}{3}\left(\frac{\Delta p}{\alpha A_o}\right)^2 + \left(\frac{\Delta p}{\alpha A_o}\right) + 1\right] + \lambda\alpha\frac{1}{5\sqrt{\pi}}\left[\left(\frac{\Delta p}{\alpha} + A_o\right)^{5/2} - A_o^{5/2}\right]\right). \tag{23}$$

From equation (23), we can easily identify the following limits:

I. The mass flow rate in the rigid wall N nanotubes with and without slips, i.e.

$1/\alpha = 0$**:** Using equation (23), the mass flow rate for the rigid tube with slips can be written as

$$(\dot{m}_{\text{rigid}})_{\text{slip}} = \lim_{1/\alpha \to 0} \left[\frac{N\rho(D_o)}{\eta(D_o)\ L} \left(\frac{\Delta p\ A_o^2}{8\pi} \left[\frac{1}{3} \left(\frac{\Delta p}{\alpha A_o} \right)^2 + \left(\frac{\Delta p}{\alpha A_o} \right) + 1 \right] + \frac{\lambda\alpha}{5\sqrt{\pi}} \left[\left(\frac{\Delta p}{\alpha} + A_o \right)^{5/2} - A_o^{5/2} \right] \right) \right], \tag{24}$$

$$\implies (\dot{m}_{\text{rigid}})_{\text{slip}} = \frac{N\rho(D_o)}{\eta(D_o)\ L} \left(\frac{\Delta p\ A_o^2}{8\pi} + \lambda \Delta p \frac{A_o^{3/2}}{2\sqrt{\pi}} \right) = \pi\ \Delta p\ \frac{N\rho(D_o)}{\eta(D_o)\ L} \left(\frac{R_o^4}{8} + \lambda \frac{R_o^3}{2} \right), \tag{25}$$

and the flow rate without slips is (i.e., using $\lambda = 0$), we get

$$(\dot{m}_{\text{rigid}})_{\text{no-slip}} = \pi\ \Delta p\ \frac{N\rho(D_o)}{\eta(D_o)\ L} \left(\frac{R_o^4}{8} \right), \tag{26}$$

which from equation (25), and (26), we get the flow enhancement E as,

$$E_{\text{rigid}} = \frac{(\dot{m}_{\text{rigid}})_{\text{slip}}}{(\dot{m}_{\text{rigid}})_{\text{no-slip}}} = \left(1 + 4\frac{\lambda}{R_o} \right) \tag{27}$$

the above expression (27) is well known and also described in Kannam et al. [24], Whitby et al. [54]. Further the flow enhancement due to deformable tubes $E_{\text{deformable}}$ can we written by using equations (23) and (26) as

$$E_{\text{deformable}} = \frac{(\dot{m}_{\text{deformable}})_{\text{slip}}}{(\dot{m}_{\text{rigid}})_{\text{no-slip}}} = \left[\frac{1}{3} \left(\frac{\Delta p}{\alpha A_o} \right)^2 + \left(\frac{\Delta p}{\alpha A_o} \right) + 1 \right] + \frac{\lambda\alpha}{\Delta p} \frac{8\pi R_o}{5} \left[\left(\frac{\Delta p}{\alpha A_o} + 1 \right)^{5/2} - 1 \right]. \tag{28}$$

To our knowledge, we have not seen the above-derived equation (28) in the literature so far. In equation (28), it's evident that the presence of additional non-linear terms, expressed as $\left(\frac{\Delta p}{\alpha A_o} \right)$, due to flexibility, results in an increase in the mass flow rate and hence the flow enhancement.

II. The mass flow rate in the deformable wall N nanotubes without slip, and without confined water properties, i.e. $\lambda = 0$, $\rho(D) = \rho_o$, $\eta(D) = \eta_o$:

$$(\dot{m}_{\text{deformable}})_{\text{no-slip}} = \frac{N\rho_o}{\eta_o\ L} \left(\frac{\Delta p\ A_o^2}{8\pi} \left[\frac{1}{3} \left(\frac{\Delta p}{\alpha A_o} \right)^2 + \left(\frac{\Delta p}{\alpha A_o} \right) + 1 \right] \right). \tag{29}$$

Equation (29) is the same as the analytical model derived by Sochi [35].

III. The mass flow rate in the rigid wall N nanotubes, without slip and without confined water properties, i.e. $1/\alpha = 0$, $\lambda = 0$, $\rho(D) = \rho_o$, $\eta(D) = \eta_o$: Under these limits, we obtain

$$\dot{m}_{\text{rigid}} = \pi\ \Delta p\ \frac{N\rho_o}{\eta_o\ L} \left(\frac{R_o^4}{8} \right), \tag{30}$$

which is a classical result of Hagen-Poiseuille flow in tubes [41, 55–57]. Now, in the following section, we will discuss the effect of deformability and slip on flow enhancement.

4.1 Enhancement and mass flow rate as a function of tube diameter

Many experimental studies suggest that the slip length varies as a function of tube diameter below 25 Å . On the other hand, the slip length is approximately constant for $D_o \geq 25$ Å [24, 53]. We show these two regions in figure 2 as I and II (in red), respectively, which are divided by the dashed blue line. In Region II, the slip length does not depend on the diameter and can be assumed constant [53]. Using the experimental parameters, such as pressure $p = 1$ bar [24, 29, 44],

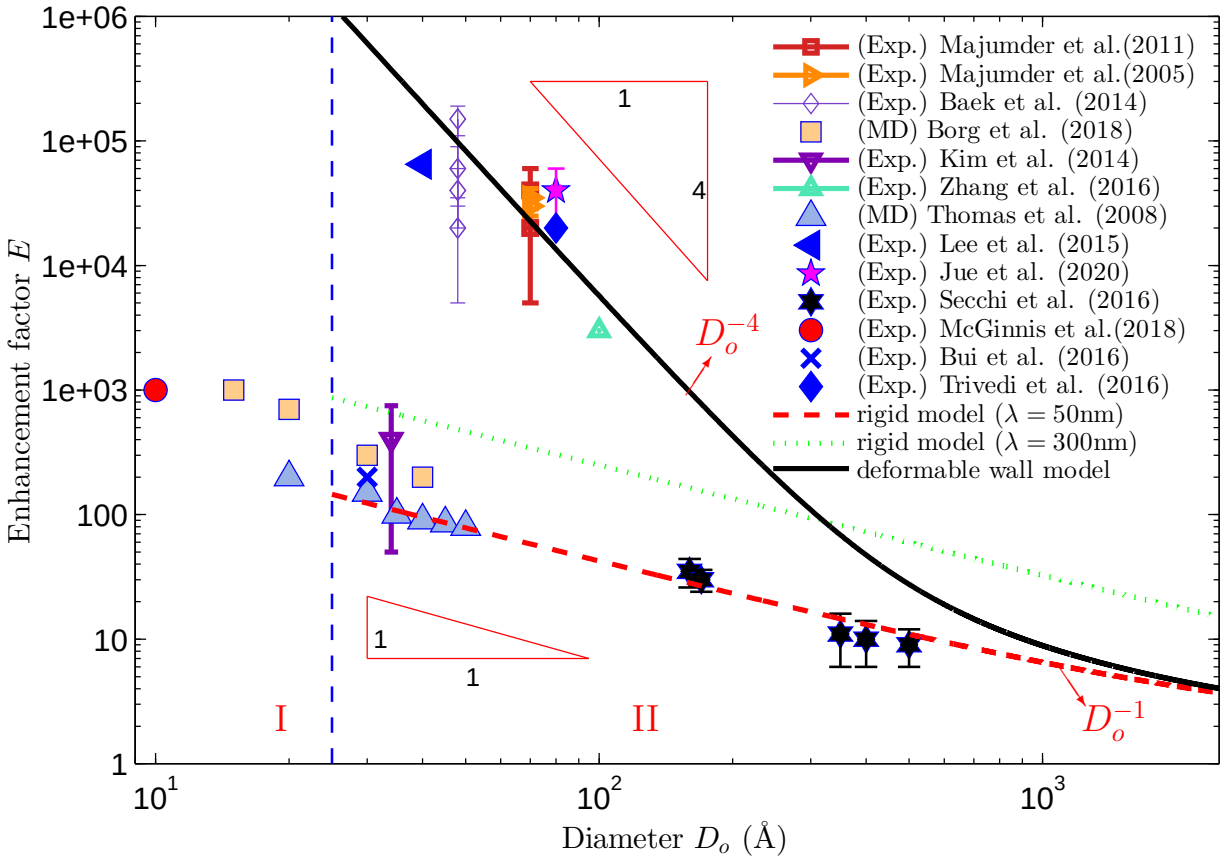

Figure 2: We show the enhancement factor using the rigid tube model (dashed red and dotted green with $\lambda = 500$ Å , and $\lambda = 3000$ Å , respectively), and the deformable tube model (solid black line) as a function of the diameter of the nano/Angstrom-sized tubes and compared with many previous experimental results and Molecular Dynamic simulation's predictions (shown with various symbols) on the log-log scale. Here, for diameter $D_o \geq 25$ Å , i.e., Region II, the slip length does not depend on the diameter and can be assumed constant [24, 53].

viscosity and density as the fitted confined water properties as described in previous section 3.3 [44], we calculated the mass flow rate by assuming the rigid wall tube for $D_o \geq 25$ Å using $\lambda = 500$ Å (shown with dashed red line), and $\lambda = 3000$ Å (shown with dotted green line), respectively. Using the calculated mass flow rate, we show the enhancement factor for the rigid tube (as described by equation (27)) as a function of the diameter of the nano/Angstrom-sized tubes in figure 2 and compared with many previous experimental results and Molecular Dynamic simulation's predictions (shown with various symbols). We further use $\alpha = 1 \times 10^{19}$ Pa/m^2 for the flexible (deformable) wall tube, and using $\lambda = 500$ Å while keeping other parameters the same as

for the rigid wall tube, we calculated the enhancement factor (by using equation (28)) as shown with the solid black line. We find that many of the experimental results and Molecular Dynamic simulation's predictions, such as the data by McGinnis et al. [8], Secchi et al. [9], Borg et al. [47], Thomas and McGaughey [48], Kim et al. [58] are well fitted with the rigid wall tube model. On the other hand, the experimental results and Molecular Dynamic simulation's predictions by Majumder et al. [23], Baek et al. [25], Zhang et al. [28], Majumder et al. [29], Majumder and Corry [30], Trivedi and Reecha [31], Lee et al. [32], Bui et al. [33] are well fitted with the deformable wall tube model.

In the later data set, researchers used a more significant pore density of the nanotube structure, which decreases the adequate thickness of the tube and hence increases the flexibility of the wall. Therefore, assuming a small deformability parameter $1/\alpha = 10^{-19}$ m^2/Pa, which describes the change in tube cross-sectional area per unit pressure difference due to the flexibility of the wall, is enough to model these results. It shows how small deformability increases the mass flow rate and, hence, the enhancement factor several times.

We find that the flow rate in the rigid tube scales as $\dot{m}_{\text{rigid}} \sim \Delta p$, whereas for the deformable tube, for negligible wall-displacement perturbation, the flow rate scales as $\dot{m}_{\text{deformable}} \sim \Delta p$ for $\left(\Delta p/\alpha A_o\right) \sim 0$, $\dot{m}_{\text{deformable}} \sim \Delta p^2$ for $\left(\Delta p/\alpha A_o\right) \sim O(10^{-1})$, and for large perturbation $\dot{m}_{\text{deformable}} \sim \Delta p^3$ for $\left(\Delta p/\alpha A_o\right) \sim O(1)$. We also find that, for a given deformability α, the percentage change in flow rate in the smaller diameter of the tube is much larger than the larger diameter of the tubes. We see in figure 2, as the tube diameter increases for the given parameters, the flow rate converges for the rigid and deformable wall tubes (shown with dashed red and solid black line for $D_o \geq 10^3$ Å). For the larger diameter of the tube, where $\left(\Delta p/\alpha A_o\right) \ll 1$, the change in flow rate scales as $(\dot{m}_{\text{deformable}} - \dot{m}_{\text{rigid}})/\dot{m}_{\text{rigid}} = \Delta\dot{m}/\dot{m} \sim (\Delta p/\alpha A_o)$, whereas for the smaller diameter of the tube, the wall perturbation due to deformity is large and the change in flow rate scales as $\sim (\Delta p/\alpha A_o)^2$. Hence, as the tube diameter decreases for the given reservoir pressure, $\Delta\dot{m}/\dot{m}$ increases A_o^{-1} (D_o^{-2}) followed by A_o^{-2} (D_o^{-4}) after a threshold with the tube diameter as shown in 2. We also find that the enhancement factor varies from $E \sim D_o^{-4}$ for $\left(\Delta p/\alpha A_o\right) \sim O(1)$ to $E \sim D_o^{-1}$ for $\left(\Delta p/\alpha A_o\right) \sim 0$ (shown with red triangle) as the tube diameter increases.

4.2 Effect of deformability on mass flow rate

We take a tube diameter $D_o = 30$ Å , the tube length $L = 1000$ Å [59], $\lambda = 500$ Å , and the confined water properties at the $D_o = 30$ Å in this section. We keep the other experimental parameters as it is and show the mass flow rate as a function of varying reservoir pressure from 0.001 Pa to 3×10^8 Pa (3000 bar) in figure 3. The data from the green line to the purple line indicate α is increasing from 10^{20} to 10^{29}, respectively. This suggests that the corresponding deformability of the tube wall is decreasing. For all data values, the nonlinear term due to flexibility varies between $\left(\Delta p/\alpha A_o\right) \sim 0$ to $\left(\Delta p/\alpha A_o\right) \sim O(1)$, where the maximum value at a given pressure occur for the green data for $\alpha = 10^{20}$. We find that for the rigid tube, where the deformability parameter is tending to zero for $\alpha = 10^{29}$, the mass flow rate varies linearly, i.e., $\dot{m}_{\text{rigid}} \sim \Delta p$ as shown with purple data in figure 3, whereas for the deformable tubes where the

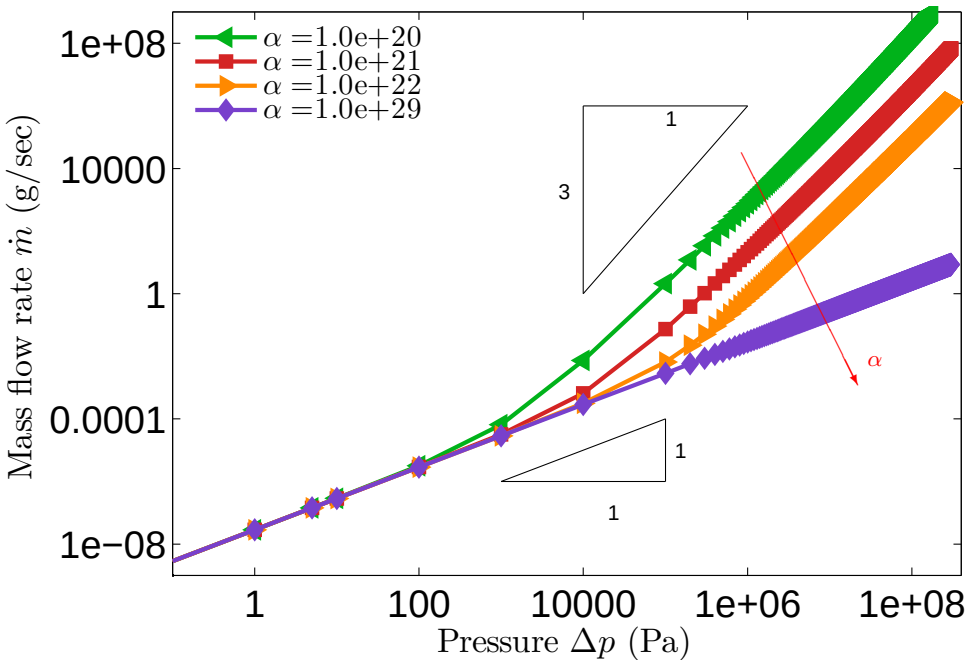

Figure 3: We show the mass flow rate as a function of varying reservoir pressure under varying deformability $(1/\alpha)$ of the tube wall on the log-log scale. The red arrow indicates the increasing values of α (corresponding decreasing value of deformability), respectively.

deformability parameter $(1/\alpha)$ is starting to get larger values from orange data to green color data, the flow rate scales as $\dot{m}_{\text{deformable}} \sim \Delta p^2$ for $\left(\Delta p/\alpha A_o\right) \sim O(10^{-1})$ during transition from $\dot{m}_{\text{rigid}} \sim \Delta p$ to $\sim \Delta p^3$, and finally to $\dot{m}_{\text{deformable}} \sim \Delta p^3$ for $\left(\Delta p/\alpha A_o\right) \sim O(1)$ as shown with the black scaling triangles in the figure 3. This suggests that the mass flow rate increases as the deformability of the tube increases.

4.3 Effect of slip on mass flow rate

We take a tube diameter $D_o = 30$ Å , the tube length $L = 1000$ Å , $\lambda = 500$ Å , and the confined water properties at the $D_o = 30$ Å in this section. From equation (23), the mass flow rate could be divided into two parts. One the mass flow in the deformable tube due to only slip and the other due to no-slip as

$$\dot{m}_1 = \frac{N\rho(R)}{\eta(R)\ L}\left(\frac{\Delta p\ A_o^2}{8\pi}\left[\frac{1}{3}\left(\lambda\alpha\frac{1}{5\sqrt{\pi}}\left[\left(\frac{\Delta p}{\alpha}+A_o\right)^{5/2}-A_o^{5/2}\right]\right)\right), \tag{31}$$

and

$$\dot{m}_2 = \frac{N\rho(R)}{\eta(R)\ L}\left(\frac{\Delta p\ A_o^2}{8\pi}\left[\frac{1}{3}\left(\frac{\Delta p}{\alpha A_o}\right)^2+\left(\frac{\Delta p}{\alpha A_o}\right)+1\right]\right), \tag{32}$$

respectively. We keep the other experimental parameters as it is and show the ratio of these mass flow rate on the linear and log-log scale as a function of varying reservoir pressure from 0.001 Pa

to 3×10^8 Pa (3000 bar) in figures 4(a), and 4(b), respectively. The data shown from the green line to the cyan line indicate α is increasing from 10^{19} Pa/m^2 to 10^{29} Pa/m^2, respectively.

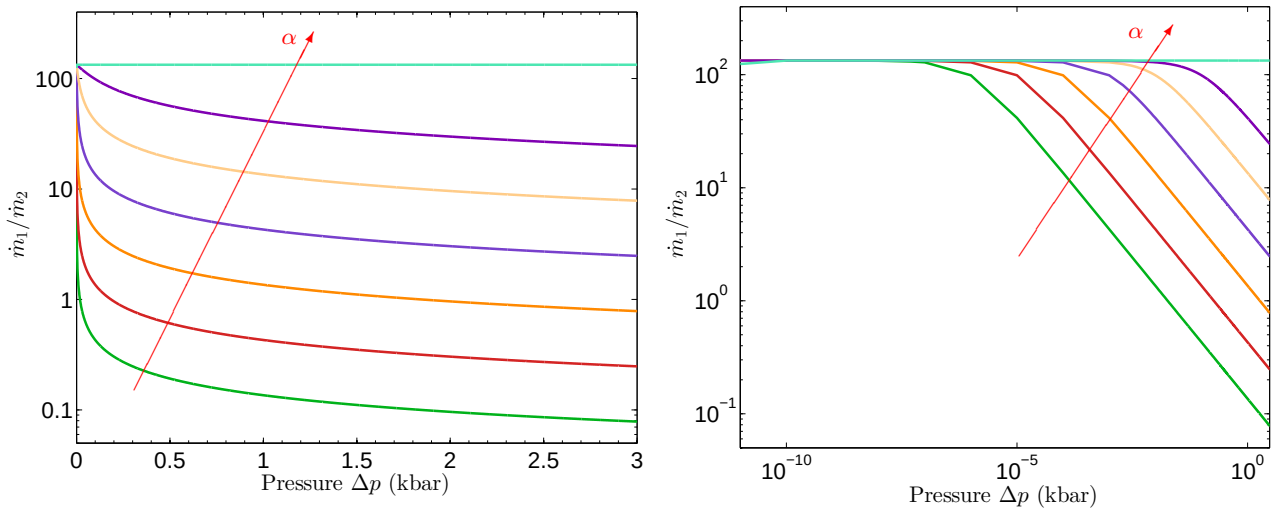

Figure 4: We show the ratio of the mass flow rate in the varying deformability of the tube due to only slip $\dot{m}_1$ and the other due to no-slip $\dot{m}_2$ as a function of varying reservoir pressure. The red arrow indicates the increasing values of α (corresponding decreasing value of deformability), respectively. In (a) and (b), the data is shown on the linear and log-log scale, respectively.

We find that for low values of α, such as for green curve $\alpha = 10^{19}$ Pa/m^2, where the deformability is greater in comparison to $\alpha = 10^{29}$ Pa/m^2 for cyan curve, the flow rate due to slip is higher in comparison to the flow due to without slip. We also find that for low pressure, the ratio remains constant irrespective of the value of the deformability parameter α. As the pressure difference increases, the ratio dependence reaches from $\dot{m}_1/\dot{m}_2 \sim \Delta p^0$ to $\Delta p^{-2.5}$. This transition starts at early pressure rise at lower value of α as shown in 4(b), where first green data curve starts to transition ($\alpha = 10^{19}$ Pa/m^2) followed by red curve ($\alpha = 10^{20}$ Pa/m^2), yellow curve ($\alpha = 10^{21}$ Pa/m^2) and finally the cyan curve remains constant for larger pressure. This trend suggests that the mass flow rate due to slips has a lower effect on the more deformable tubes than on the less deformable or rigid tubes.

4.4 Effect of deformability and slip of graphene sheet on the mass flow rate

In this section, we take tube diameter $D_o = 30$ Å and the confined water properties at the same diameter. We use $1/\alpha = 0$ m^2/Pa for rigid tubes and $1/\alpha = 10^{-18}$ for deformable tubes. We keep the other experimental parameters as it is and show the mass flow rate for the deformable tube ($1/\alpha = 10^{-18}$ m^2/Pa) with slip (i.e., $\lambda = 500$ Å) in green color, mass flow rate for the deformable tube ($1/\alpha = 10^{-18}$ m^2/Pa) without slip (i.e., $\lambda = 0$ Å) in red color, mass flow rate for the rigid wall tube ($1/\alpha = 0$ m^2/Pa) with slip (i.e., $\lambda = 500$ Å) in yellow color, and mass flow rate for the rigid wall tube ($1/\alpha = 0$ m^2/Pa) without slip (i.e., $\lambda = 0$ Å) in purple color in figure 5 as a function of varying pressure, respectively.

We find that the deformability of the wall increases the mass flow rate at all varying pressure

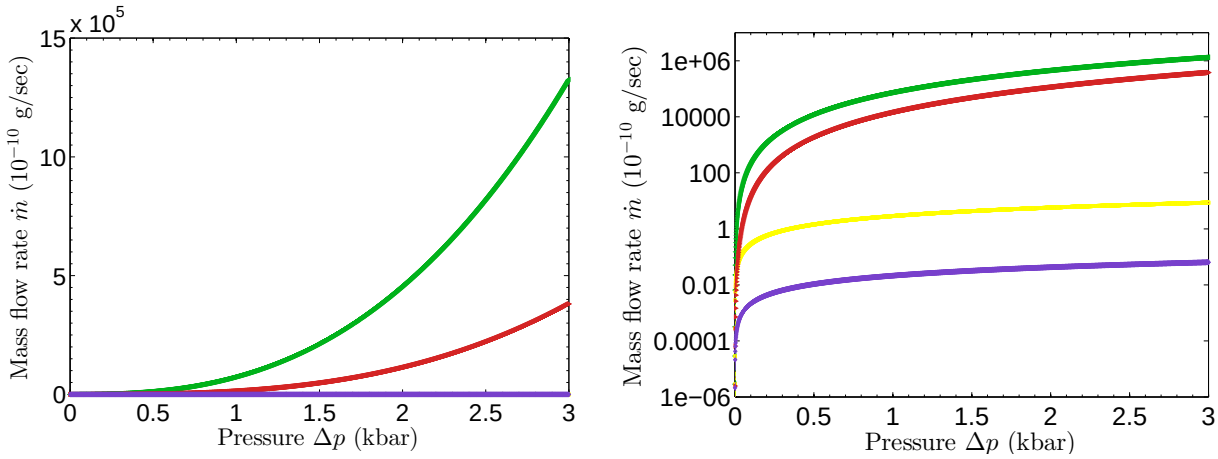

Figure 5: We show the mass flow rate in the rigid and deformable tubes with and without slips as a function of varying reservoir pressure. In (a) and (b), the data is shown on the linear and semilog scale, respectively. The data shown are the mass flow rate for the deformable tube ($1/\alpha = 10^{-18}$ m^2/Pa) with slip (i.e., $\lambda = 500$ Å) in green color, mass flow rate for the deformable tube ($1/\alpha = 10^{-18}$ m^2/Pa) without slip (i.e., $\lambda = 0$ Å) in red color, mass flow rate for the rigid wall tube ($1/\alpha = 0$ m^2/Pa) with slip (i.e., $\lambda = 500$ Å) in yellow color, and mass flow rate for the rigid wall tube ($1/\alpha = 0$ m^2/Pa) without slip (i.e., $\lambda = 0$ Å) in purple color, respectively.

fields compared to the rigid wall tube, as shown with green and red data lines. We find that for $\Delta p = 3$ kbar, the mass flow rate in the rigid tube wall with slips (yellow) is 8.3x10^{-10} g/s, whereas for the deformable tube with slips (green), it is 1.2x10^{-4} g/s. Therefore, slight deformability in the tube increases the mass flow rate by approximately an order of 10^5 times, which is significant. We further find that the difference between mass flow rate with slips and without slips for both deformable tubes (with and without slip) and rigid wall tubes (with and without tubes) are of order 10^2 times. This shows that although slip increases the flow rate in nanotubes, the deformability has a larger effect in increasing the mass flow rate. Finally, the summary of figure 5 says the lowest mass flow rate is for rigid wall tubes without slips, then incremented for rigid wall tubes with slips, further increment for deformable wall tubes without slips, and the most significant mass flow rate for deformable wall tube with slips for the given parameters.

We also find that as the magnitude of the pressure increases in a deformable tube, the flow rate also increases significantly compared to the rigid tube. The reason is that in the case of a rigid tube, the mass flow rate is linearly proportional to Δp. On the other hand, in the case of the deformable tube, the flow rate (from equation (23)) consists of non-linear terms of Δp, where it starts to increase from Δp to Δp^3 as pressure increases.

5 Conclusion

In this paper, we derived a model for the mass flow rate in the rigid and deformable nano/Angstrom-size tubes for the nanoconfined water/fluid transport by using the small displacement structural mechanics through a linear pressure-area relationship as presented by Sochi [35] under the lubrication approximation. For the validation purpose, we show that the newly derived model also

describes the flow dynamics of Newtonian fluids under different conditions as its limiting cases, which have been previously reported in the literature [24, 35, 54–57]. Thorough validation tests have revealed that the newly derived model produce mathematically and physically sensible flow rate in diverse situations of applied pressure, deformability, shallow tube geometry, and boundary conditions in the nanotubes. We also compare the predictions by our deformable-wall and rigid-wall model with the experimental results and the MD simulation predictions by multiple literatures. We find that many studies, as shown in figure 2, were well-predicted by the rigid-wall model with slips [8, 9, 47, 48, 58]. However, there are many studies with high porosity and thin wall tubes, where elasticity or deformability of the tube is essential in modelling were well-predicted by the deformable-wall model with slips [23, 25, 28–33].

In our study, we focus on investigating the impact of two key factors: the deformability of the nanotubes and the slip length on the flow rate. We find that as the deformability $1/\alpha$ increases (or corresponding thickness $\mathcal{T}$ and elastic modulus E of the wall decreases), the flow rate inside the tube increases. We find that the flow rate in deformable tubes scales as $\dot{m}_{\text{deformable}} \sim 1/\alpha^0$ for $\left(\Delta p/\alpha A_o\right) \ll 1$, $\dot{m}_{\text{deformable}} \sim 1/\alpha$ for $\left(\Delta p/\alpha A_o\right) \sim O(10^{-1})$ and $\dot{m}_{\text{deformable}} \sim \alpha^2$ for $\left(\Delta p/\alpha A_o\right) \sim O(1)$. We also find that, for a given deformability factor α, the percentage change in flow rate in the smaller diameter of the tube is much larger than the larger diameter. As the tube diameter decreases for the given reservoir pressure, $\Delta\dot{m}/\dot{m}$ increases A_o^{-1} followed by A_o^{-2} after a threshold with the tube diameter.

We further find that for the rigid tube, where the deformability parameter $1/\alpha = 0$, the mass flow rate varies linearly, i.e., $\dot{m}_{\text{rigid}} \sim \Delta p$, whereas for the deformable tubes, the flow rate scales as $\dot{m}_{\text{deformable}} \sim \Delta p^2$ for $\left(\Delta p/\alpha A_o\right) \sim O(10^{-1})$ during transition from $\dot{m}_{\text{rigid}} \sim \Delta p$ to $\sim \Delta p^3$, and finally to $\dot{m}_{\text{deformable}} \sim \Delta p^3$ for $\left(\Delta p/\alpha A_o\right) \sim O(1)$.

We further find that the slip also plays a significant role in increasing the mass flow rate in the nanotubes. Still, the deformability has, in comparison, a more substantial effect in increasing the mass flow rate to several orders than the slips.

6 Acknowledgements

We thank Mehdi Neek-Amal and Amritha Janardanan for the fruitful discussion on the subject.

References

[1] GQ Max Lu and Xiu Song Zhao. *Nanoporous materials: science and engineering*, volume 4. World Scientific, 2004.

[2] Alyson Sagle and Benny Freeman. Fundamentals of membranes for water treatment. *The future of desalination in Texas*, 2(363):137, 2004.

[3] Elton Oyarzua, Jens H Walther, Andrés Mejía, and Harvey A Zambrano. Early regimes of water capillary flow in slit silica nanochannels. *Physical Chemistry Chemical Physics*, 17(22):14731–14739, 2015.

[4] Zohreh Jalilvand, Farzin Zokaee Ashtiani, Amir Fouladitajar, and Hamid Rezaei. Computational fluid dynamics modeling and experimental study of continuous and pulsatile flow in flat sheet microfiltration membranes. *Journal of Membrane Science*, 450:207–214, 2014.

[5] Fatemeh Ebrahimi, Farzaneh Ramazani, and Muhammad Sahimi. Nanojunction effects on water flow in carbon nanotubes. *Scientific Reports*, 8(1):7752, 2018.

[6] Pranay Ashok Asai. *Assessing Fluid Flow in Nanoporous Media and Doublet Multi-Fractured Enhanced Geothermal Systems*. PhD thesis, The University of Utah, 2021.

[7] Jürgen Köfinger, Gerhard Hummer, and Christoph Dellago. Macroscopically ordered water in nanopores. *Proceedings of the National Academy of Sciences*, 105(36):13218–13222, 2008.

[8] Robert L McGinnis, Kevin Reimund, Jian Ren, Lingling Xia, Maqsud R Chowdhury, Xuanhao Sun, Maritza Abril, Joshua D Moon, Melanie M Merrick, Jaesung Park, et al. Large-scale polymeric carbon nanotube membranes with sub–1.27-nm pores. *Science advances*, 4(3):e1700938, 2018.

[9] Eleonora Secchi, Sophie Marbach, Antoine Niguès, Derek Stein, Alessandro Siria, and Lydéric Bocquet. Massive radius-dependent flow slippage in carbon nanotubes. *Nature*, 537(7619):210–213, 2016.

[10] Adrijana Filipović. Water plant and soil relation under stress situations. *Soil moisture importance*, 73, 2020.

[11] Sisi Cao, Priya Rathi, Xuanhao Wu, Deoukchen Ghim, Young-Shin Jun, and Srikanth Singamaneni. Cellulose nanomaterials in interfacial evaporators for desalination: a "natural" choice. *Advanced Materials*, 33(28):2000922, 2021.

[12] Hiroto Kawagishi, Shun-ichi Funano, Yo Tanaka, and Yan Xu. Flexible glass-based hybrid nanofluidic device to enable the active regulation of single-molecule flows. *Nano Letters*, 23(6):2210–2218, 2023.

[13] Xueye Chen and Lei Zhang. Review in manufacturing methods of nanochannels of bio-nanofluidic chips. *Sensors and Actuators B: Chemical*, 254:648–659, 2018.

[14] Anastasios Economou, Christos Kokkinos, and Mamas Prodromidis. Flexible plastic, paper and textile lab-on-a chip platforms for electrochemical biosensing. *Lab on a Chip*, 18(13):1812–1830, 2018.

[15] Fangsheng Wu, Jiaping Lin, Liquan Wang, and Shaoliang Lin. Polymer vesicles in a nanochannel under flow fields: a dpd simulation study. *Macromolecular Theory and Simulations*, 31(5):2200027, 2022.

[16] Meijiao Zhao, Wanhao Wu, and Bin Su. ph-controlled drug release by diffusion through silica nanochannel membranes. *ACS applied materials & interfaces*, 10(40):33986–33992, 2018.

[17] Shuping Jiao and Mingchao Liu. Snap-through in graphene nanochannels: With application to fluidic control. *ACS Applied Materials & Interfaces*, 13(1):1158–1168, 2020.

[18] Yi Han, Zhen Xu, and Chao Gao. Ultrathin graphene nanofiltration membrane for water purification. *Advanced Functional Materials*, 23(29):3693–3700, 2013.

[19] Pranay Chakraborty, Tengfei Ma, Lei Cao, and Yan Wang. Significantly enhanced convective heat transfer through surface modification in nanochannels. *International Journal of Heat and Mass Transfer*, 136:702–708, 2019.

[20] Jie Sun, Yaling He, Wenquan Tao, Xin Yin, and Huasheng Wang. Roughness effect on flow and thermal boundaries in microchannel/nanochannel flow using molecular dynamics-continuum hybrid simulation. *International journal for numerical methods in engineering*, 89(1):2–19, 2012.

[21] Tristan da Câmara Santa Clara Gomes, Flavio Abreu Araujo, and Luc Piraux. Making flexible spin caloritronic devices with interconnected nanowire networks. *Science advances*, 5(3):eaav2782, 2019.

[22] Vidit Sharma and Ashish Garg. Numerical investigation of effects of compound angle and length to diameter ratio on adiabatic film cooling effectiveness. *arXiv preprint arXiv:1405.0560*, 2014.

[23] Mainak Majumder, Nitin Chopra, Rodney Andrews, and Bruce J Hinds. Enhanced flow in carbon nanotubes. *Nature*, 438(7064):44–44, 2005.

[24] Sridhar Kumar Kannam, BD Todd, Jesper Schmidt Hansen, and Peter J Daivis. How fast does water flow in carbon nanotubes? *The Journal of chemical physics*, 138(9), 2013.

[25] Youngbin Baek, Cholin Kim, Dong Kyun Seo, Taewoo Kim, Jeong Seok Lee, Yong Hyup Kim, Kyung Hyun Ahn, Sang Seek Bae, Sang Cheol Lee, Jaelim Lim, et al. High performance and antifouling vertically aligned carbon nanotube membrane for water purification. *Journal of membrane Science*, 460:171–177, 2014.

[26] Ashish Garg and Pranjal Prasad. Yield-stress shear thinning and shear thickening fluid flows in deformable channels. *ChemRxiv-Polymer Science, DOI: 10.26434/chemrxiv-2023-jb7xw*, pages 1–19, 2023.

[27] Ashish Garg and Pranjal Prasad. Wall-slip effects on the yield-stress fluid flows in the rigid and deformable channel. *ChemRxiv-Polymer Science, DOI: 10.26434/chemrxiv-2023-l3knn*, pages 1–30, 2023.

[28] Xiuyin Zhang, Chuanzhuang Zhao, Nanping Xiang, and Wei Li. Chain entanglements and hydrogen bonds in carbopol microgel reinforced hydrogel. *Macromolecular Chemistry and Physics*, 217(19):2139–2144, 2016.

[29] Mainak Majumder, Nitin Chopra, and Bruce J Hinds. Mass transport through carbon nanotube membranes in three different regimes: ionic diffusion and gas and liquid flow. *ACS nano*, 5(5):3867–3877, 2011.

[30] Mainak Majumder and Ben Corry. Anomalous decline of water transport in covalently modified carbon nanotube membranes. *Chemical Communications*, 47(27):7683–7685, 2011.

[31] Monika Trivedi and K Reecha. Recent development and applications of carbon nanotubes. *Chem. Sci. Rev. Lett*, 9: 502–510, 2020.

[32] Byeongho Lee, Youngbin Baek, Minwoo Lee, Dae Hong Jeong, Hong H Lee, Jeyong Yoon, and Yong Hyup Kim. A carbon nanotube wall membrane for water treatment. *Nature communications*, 6(1):7109, 2015.

[33] Ngoc Bui, Eric R Meshot, Sangil Kim, José Peña, Phillip W Gibson, Kuang Jen Wu, and Francesco Fornasiero. Ultrabreathable and protective membranes with sub-5 nm carbon nanotube pores. *Advanced Materials*, 28(28):5871–5877, 2016.

[34] Xiluan Wang and Gaoquan Shi. Flexible graphene devices related to energy conversion and storage. *Energy & Environmental Science*, 8(3):790–823, 2015.

[35] Taha Sochi. The flow of newtonian and power law fluids in elastic tubes. *International Journal of Non-Linear Mechanics*, 67:245–250, 2014.

[36] Ashish Garg. Pulsatile pressure enhanced rapid water transport through flexible graphene nano/angstrom-size channels: a continuum modeling approach using the micro-structure of nanoconfined water. *New Journal of Physics*, 25 (10):103024, 2023. doi: 10.1088/1367-2630/acff7e.

[37] CLMH Navier. Mémoire sur les lois du mouvement des fluides. *Mémoires de l'Académie Royale des Sciences de l'Institut de France*, 6(1823):389–440, 1823.

[38] Miccal T. Matthews and James M. Hill. Nano boundary layer equation with nonlinear navier boundary condition. *Journal of Mathematical Analysis and Applications*, 333(1):381 – 400, 2007. ISSN 0022-247X. doi: https://doi.org/10.1016/j.jmaa.2006.08.047.

[39] Jaroslav Hron, C Le Roux, Josef Málek, and KR Rajagopal. Flows of incompressible fluids subject to navier's slip on the boundary. *Computers & Mathematics with Applications*, 56(8):2128–2143, 2008.

[40] Charles Edward Fisher. The effects of a navier-slip boundary condition on the flow of two immiscible fluids in a microchannel. 2013.

[41] Ashish Garg. Aerodynamics. In *GATE Aerospace Forum Educational Services*, 2015.

[42] Ashish Garg, Nico Bergemann, Beccy Smith, Matthias Heil, and Anne Juel. Fluidisation of yield stress fluids under vibration. *Science Talks*, 3:100067, 2022.

[43] Barry James Cox and James Murray Hill. Flow through a circular tube with a permeable navier slip boundary. *Nanoscale research letters*, 6:1–9, 2011.

[44] Hongfei Ye, Hongwu Zhang, Zhongqiang Zhang, and Yonggang Zheng. Size and temperature effects on the viscosity of water inside carbon nanotubes. *Nanoscale research letters*, 6:1–5, 2011.

[45] Feng Du, Liangti Qu, Zhenhai Xia, Lianfang Feng, and Liming Dai. Membranes of vertically aligned superlong carbon nanotubes. *Langmuir*, 27(13):8437–8443, 2011.

[46] Jason Knowles Holt. Methods for probing water at the nanoscale. *Microfluidics and Nanofluidics*, 5(4):425–442, 2008.

[47] Matthew K Borg, Duncan A Lockerby, Konstantinos Ritos, and Jason M Reese. Multiscale simulation of water flow through laboratory-scale nanotube membranes. *Journal of Membrane Science*, 567:115–126, 2018.

[48] John A Thomas and Alan JH McGaughey. Reassessing fast water transport through carbon nanotubes. *Nano letters*, 8(9):2788–2793, 2008.

[49] Sony Joseph and NR Aluru. Why are carbon nanotubes fast transporters of water? *Nano letters*, 8(2):452–458, 2008.

[50] Ashish Garg. Fluidisation of yield stress materials under vibration. *PhD thesis, The University of Manchester*, pages 1–175, 2022.

[51] Praveen Chandrashekar and Ashish Garg. Vertex-centroid finite volume scheme on tetrahedral grids for conservation laws. *Computers & Mathematics with Applications*, 65(1):58–74, 2013.

[52] Ashish Garg, Nico Bergemann, Beccy Smith, Matthias Heil, and Anne Juel. Fluidisation of yield stress fluids under vibration. *Journal of Non-Newtonian Fluid Mechanics*, 294:104595, 2021.

[53] Ashish Garg and Swati Bishnoi. An empirical experimental observations and md simulation data-based model for the material properties of confined fluids in nano/angstrom size tubes. 2023. doi: 10.26434/chemrxiv-2023-s66r8.

[54] Max Whitby, Laurent Cagnon, Maya Thanou, and Nick Quirke. Enhanced fluid flow through nanoscale carbon pipes. *Nano letters*, 8(9):2632–2637, 2008.

[55] Frank M White. *Fluid mechanics*. New York, 1990.

[56] George Keith Batchelor. *An introduction to fluid dynamics*. Cambridge university press, 1967.

[57] Brian J Kirby. *Micro-and nanoscale fluid mechanics: transport in microfluidic devices*. Cambridge university press, 2010.

[58] Sangil Kim, Francesco Fornasiero, Hyung Gyu Park, Jung Bin In, Eric Meshot, Gabriel Giraldo, Michael Stadermann, Micha Fireman, Jerry Shan, Costas P Grigoropoulos, et al. Fabrication of flexible, aligned carbon nanotube/polymer composite membranes by in-situ polymerization. *Journal of membrane science*, 460:91–98, 2014.

[59] B Radha, A Esfandiar, FC Wang, AP Rooney, K Gopinadhan, A Keerthi, A Mishchenko, A Janardanan, P Blake, L Fumagalli, et al. Molecular transport through capillaries made with atomic-scale precision. *Nature*, 538(7624): 222–225, 2016.